Physics-Inspired Continuous Transformer for Fast QDSA Reconstruction

Yang Liu[1,2], Zehua Liu[3], Xiangyun Liao[2], Chuanzhi Duan[4(✉)], and Weixin Si[2(✉)]

[1]Southern University of Science and Technology, China
[2]Shenzhen University of Advanced Technology, China
[3]Beihang University, China
[4]Zhujiang Hospital, Southern Medical University, China
siweixin@suat-sz.edu.cn, doctor_duanzj@163.com

Abstract. Intra-operative endovascular treatment of intracranial aneurysms calls for rapid and reliable hemodynamic quantification. Angiographic Parametric Imaging (API) is derived from DSA time–density curves (TDCs), yet irregular frame rates and dose-reduction gaps often make conventional pixel-wise Gamma-variate fitting unstable and computationally expensive. We propose PIC-Former, a physics-inspired continuous transformer that reconstructs a physiologically plausible TDC function $\hat{c}(t)$ from irregular DSA samples. PIC-Former uses Δt-aware causal attention for inter-frame gaps and physics-inspired regularization to encourage valid contrast arrival, peak, and washout dynamics. On 52 paired DSA–4D Flow MRI cases and an independent 11-case CFD cohort, QDSA velocities computed from the reconstructed TDCs achieve relative MAEs of 3.1% and 2.01%, respectively, outperforming Gamma-variate fitting (11.8% on DSA–4D Flow MRI). PIC-Former generates full-field parametric maps for a complete DSA run in 12.45 s and remains stable under a 20% frame-drop stress test. In a retrospective intra-operative risk stratification study, the proposed pipeline improves stratification accuracy from 87.5% to 95.0% compared to the Gamma-variate-based baseline. The code and reproducibility test set is available at https://github.com/LY-SUSTech/PIC-Former.git.

Keywords: Intracranial aneurysm · Angiographic parametric imaging · Physics-inspired continuous transformer · Hemodynamic assessment · Intra-operative risk stratification

1 Introduction

Intracranial aneurysm (IA) is routinely treated by endovascular intervention under 2D Digital Subtraction Angiography (DSA) guidance [?, ?, ?, ?]. Intra-operative decisions would benefit from hemodynamic quantification. However, established options (4D Flow MRI, computed tomography perfusion (CTP),

(✉) Corresponding author

and computational fluid dynamics (CFD)) are impractical in the intra-operative setting due to their reliance on dedicated scanners, prolonged acquisitions, or expensive simulations [**?**, **?**]. As the intra-operative clinical standard, DSA is widely available but offers only limited functional assessment. Angiographic Parametric Imaging (API) bridges this gap by converting DSA time–density curves (TDCs) into full-field pseudo-color perfusion maps from routine angiography [**?**, **?**], a direction also known as perfusion DSA [**?**, **?**].

However, API hinges on robust TDC reconstruction under irregular sampling, complementary to DSA frame-interpolation methods that recover high-frame-rate sequences in the image domain [**?**, **?**]. Conventional API relies on Gamma-variate fitting and per-pixel non-linear optimization, which become unstable or slow with sampling gaps. Recent mixture models and deep continuous temporal models increase flexibility [**?**, **?**, **?**, **?**, **?**], yet physiological violations can still bias timing parameters and contaminate downstream velocity estimates. Therefore, intra-operative API requires a fast, sampling-robust, and clinically interpretable reconstruction approach in which derived curves can be inspected per ROI.

To meet these requirements, we introduce PIC-Former, a physics-inspired continuous transformer that reconstructs a continuous temporal TDC function $\hat{c}(t)$ from irregularly sampled DSA. By conditioning attention on inter-frame gaps and introducing DSA-specific contrast-kinetic regularization, rather than PDE residuals, PIC-Former improves sampling robustness and yields physiologically plausible arrival/peak/washout dynamics. The reconstructed curves support fast full-field API mapping and facilitate comparison between pre-operative and intra-operative hemodynamics. Moreover, quantitative DSA (QDSA) velocities derived via shifted least squares serve as an objective endpoint for cross-modal validation against 4D Flow MRI and CFD.

This work makes three contributions: (1) a timestamp-conditioned, Δt-aware transformer for fast, sampling-robust TDC reconstruction as the fitting engine for API; (2) cross-modal validation of QDSA velocities derived from reconstructed TDCs using paired DSA–4D Flow MRI and patient-specific CFD simulations; and (3) a retrospective intra-operative risk stratification study using API-derived change features during IA interventions.

2 Method

Fig. **??** illustrates the proposed pipeline: irregular DSA TDC samples with acquisition timestamps are reconstructed by PIC-Former into continuous temporal curves $\hat{c}(t)$, which then support full-field API map generation (time-to-peak (TTP), cerebral blood flow (CBF), cerebral blood volume (CBV), mean transit time (MTT)) and QDSA velocity estimation via shifted least squares (SLS).

2.1 Δt-Aware Causal Attention for Temporal Reconstruction

Within a contrast window $[t_s, t_e]$, each ROI TDC is observed as irregular samples $\{(t_i, c_i)\}_{i=1}^{T}$. PIC-Former outputs a continuous temporal function $\hat{c}(t)$ for $t \in$

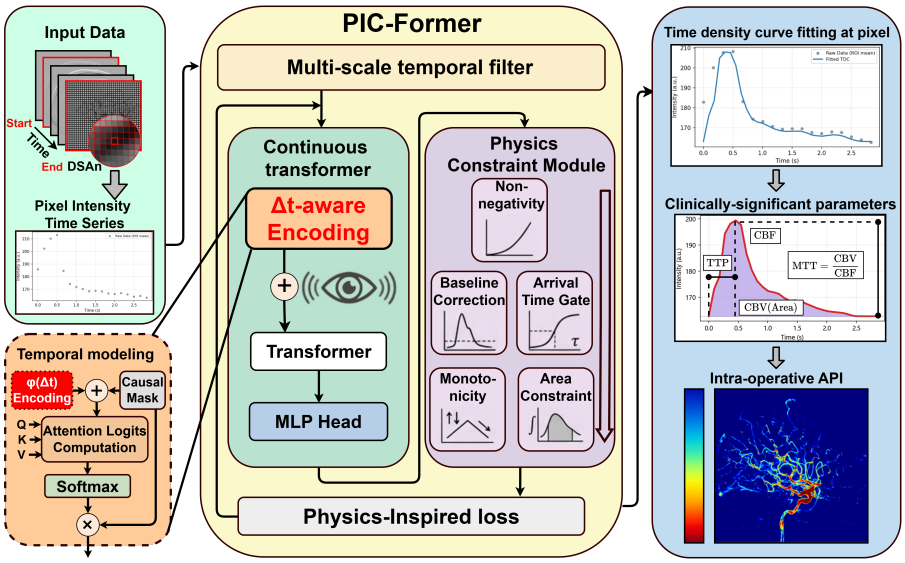

Fig. 1. Overview of PIC-Former and the downstream intra-operative quantification pipeline: irregular DSA samples are reconstructed into continuous temporal TDCs, which then support API perfusion maps and SLS QDSA velocity estimation.

$[t_s, t_e]$, evaluated on a uniform temporal grid for API map computation and SLS delay/velocity estimation between proximal–distal ROIs separated by calibrated distance Δx; segments with large SLS residuals are rejected.

To capture distinct contrast passage phases (arrival, peak, washout) under irregular sampling, PIC-Former builds a multi-scale temporal representation. Each sample is first embedded by combining an intensity encoding of c_i with a continuous temporal encoding of timestamps [**?**, **?**, **?**]. We then aggregate local and longer-range context through a multi-scale temporal filter that pools samples over several temporal receptive fields (Fig. **??**) before applying attention, enabling the model to handle heterogeneous time gaps across different contrast phases.

To explicitly model irregular time intervals, we parameterize causal attention with inter-frame gaps $\Delta t_{ij} = t_i - t_j$ rather than positional indices. Let $\mathbf{q}_i$ and $\mathbf{k}_j$ denote query and key vectors; the attention score is:

$$s_{ij} = \frac{\mathbf{q}_i^\top \mathbf{k}_j}{\sqrt{d}} + \phi(\Delta t_{ij}), \tag{1}$$

where $\phi(\cdot)$ is a learnable kernel (a small MLP) that maps real-valued Δt_{ij} to head-wise biases, so the temporal prior varies smoothly with sampling gaps and generalizes across different acquisition intervals. A causal mask prevents future-frame leakage for intra-operative use.

2.2 Physics-Inspired Constraints

Under sparse observations, unconstrained regressors may interpolate samples while violating tracer kinetics, biasing timing indices and destabilizing delay estimation. We incorporate soft physics-inspired constraints via regularization:

$$\mathcal{L} = \mathcal{L}_{\text{rec}} + \lambda \mathcal{L}_{\text{pi}}, \tag{2}$$

where $\mathcal{L}_{\text{rec}}$ is mean squared error on observed samples. The physics-inspired regularization $\mathcal{L}_{\text{pi}}$ decomposes into terms with direct physiological meaning: non-negativity enforces valid concentration; baseline suppression and an arrival-time gate encode pre-bolus quiescence and discourage premature onset; a smoothness prior suppresses non-physical oscillations; and an area-related term stabilizes CBV estimation. Because these constraints are defined in the original time–density domain and can be inspected per ROI, the reconstruction remains inspectable at each step (samples, constrained curve, and derived perfusion/velocity metrics), rather than relying on an opaque black-box mapping.

2.3 API Parameters and SLS Velocity Estimation

From each reconstructed curve $\hat{c}(t)$, we compute API parameters commonly used in perfusion analysis [**?**]:

$$\text{CBV} = \int_0^\infty \hat{c}(t)\, dt. \tag{3}$$

$$\text{TTP} = \arg\max_t \hat{c}(t). \tag{4}$$

Since DSA acquisitions span a finite contrast window $[t_s, t_e]$, we approximate $\int_0^\infty \hat{c}(t)\, dt$ by $\int_{t_s}^{t_e} \hat{c}(t)\, dt$ after baseline suppression.

For segment velocities, shifted least squares (SLS) [**?**, **?**] estimates transit delay between proximal and distal ROI curves $\hat{c}_p(t)$ and $\hat{c}_d(t)$:

$$\hat{\tau} = \arg\min_{\tau \in [\tau_{\min}, \tau_{\max}]} \sum_k \left(\hat{c}_p(t_k) - \hat{c}_d(t_k + \tau)\right)^2, \tag{5}$$

where $\hat{c}_d(t_k + \tau)$ is obtained by evaluating the continuous downstream curve at the shifted timestamp $t_k + \tau$. With calibrated distance Δx (mm) and $\hat{\tau}$ (s), segment velocity is $v = \Delta x / \hat{\tau}$. When multiple ROI pairs along a segment are available, we additionally fit a linear model to delays as a function of distances and report the segment velocity as the inverse slope for improved robustness.

3 Experiment

3.1 Dataset

For this study, we constructed three complementary cohorts: a paired DSA–4D Flow MRI cohort (52 cases) for cross-modal velocity validation, an 11-case

patient-specific CFD cohort for mechanistic evaluation, and a separate 40-case retrospective outcome cohort for intra-operative risk stratification based on API-derived change features.

We selected 52 internal carotid artery (ICA) aneurysm cases (mean age 54.6 years; 37 female and 15 male patients) with paired intra-operative DSA and post-operative 4D Flow MRI acquired within 48 hours for hemodynamic validation [**?**, **?**]. Each case comprised more than 20 effective frames at a resolution of 750×750 (8-bit TDCs read from 12-bit DICOM), acquired at 4/6/8 fps (mean 5.62 fps) and spanning arterial arrival to a physician-confirmed pre-venous-sinus filling endpoint rather than the arterial phase alone. Inclusion criteria included standard power-injector injection (5 mL at 9 mL/s), biplane acquisition, complete bolus passage, and geometric calibration (Δx uncertainty ± 0.5 mm); runs or frames with severe motion, bolus contamination, incomplete passage, missing calibration, or insufficient effective frames were excluded, and timestamped pixel-wise TDCs were then extracted from the contrast-subtracted sequences as model input. A neuroradiologist delineated 2–5 vessel segments per case on co-registered images, with ground-truth velocities extracted from 4D Flow phase-contrast centerlines. The cohort was split at case level into 3:1:1 (train/val/test), stratified by aneurysm location. Eleven geometrically complex cases underwent patient-specific CFD simulation (3D rotational angiography, 0.1 mm mesh, pulsatile inlet at 15 cm/s) [**?**] for independent SLS QDSA validation [**?**, **?**] and were excluded from training. We assembled a separate 40-case intra-operative risk stratification cohort from 391 DICOM sequences (23 females/17 males; age 36–71 years; mean 52.2 years), comprising 25 complication-free cases, 7 ischemic cases with diffusion-weighted imaging (DWI) confirmation within 72 h, and 8 computed tomography (CT)-confirmed hemorrhagic events, to assess sensitivity to hemodynamic changes by comparing pre-operative and intra-operative API parameters across anatomical ROIs (aneurysm sac, parent artery, middle cerebral artery (MCA)/anterior cerebral artery (ACA) territories) [**?**].

3.2 Implementation Details

We implemented PIC-Former in PyTorch on an NVIDIA RTX 4090 GPU. The model was trained using the AdamW optimizer with a learning rate of 1×10^{-3} and batch size of 64 for up to 50 epochs, with early stopping based on validation set performance. Physiological plausibility was enforced through the differentiable physics-inspired regularization defined in Section 2.2, whose weight λ was selected on the validation set. All baseline methods adhered to their original hyperparameter configurations when applicable.

3.3 Evaluation and Hemodynamic Consistency

We benchmarked PIC-Former against Gamma-variate fitting, N-GMM [**?**], non-parametric smoothers (Savitzky–Golay, LOWESS), and deep sequence models (LSTM/Transformer) with and without physics-inspired constraints. Performance was assessed from three complementary perspectives: (1) relative QDSA

Table 1. Quantitative comparison of TDC (8-bit) reconstruction and hemodynamic consistency. "4D Flow" and "CFD" report relative QDSA velocity MAE (%) against reference standards; "MAE" denotes pointwise TDC reconstruction error. "Time" is the wall-clock runtime to generate full-field parametric maps for one complete DSA run on an RTX 4090 GPU.

Method	4D Flow (%)	CFD (%)	MAE	Time (s)
Gamma-variate	11.8	6.70	3.139	268.27
Gamma-variate (Drop-20%)	14.5	8.07	4.102	711.90
N-GMM	13.6	7.61	5.851	128.41
Savitzky–Golay	10.4	5.98	2.440	4.23
LOWESS	9.8	5.67	2.070	3.32
LSTM	8.6	5.13	0.316	8.62
PI-LSTM	5.2	3.36	1.296	8.69
PI-LSTM (Drop-20%)	6.0	3.84	1.459	8.69
Transformer	7.5	4.55	**0.273**	13.85
PI-Transformer	4.3	2.70	1.227	13.90
PI-Transformer (Drop-20%)	4.9	3.04	1.352	13.90
PIC-Former w/o PI	6.8	4.19	0.342	41.78
PIC-Former w/o Δt	5.6	3.62	1.122	**1.96**
PIC-Former (Drop-20%)	3.4	2.19	1.025	41.93
PIC-Former (full)	**3.1**	**2.01**	0.958	12.45

velocity mean absolute error (MAE) against 4D Flow MRI and CFD references to quantify hemodynamic consistency—the clinically actionable target; (2) pointwise TDC reconstruction MAE to evaluate waveform fidelity; and (3) end-to-end runtime for full-field parametric map generation.

As summarized in Table **??**, PIC-Former improves hemodynamic consistency and runtime. Compared to Gamma-variate fitting, PIC-Former reduces velocity MAE against 4D Flow and CFD references by 8.7 and 4.69 percentage points, respectively. Relative to the strongest physics-inspired deep baseline (PI-Transformer), PIC-Former further reduces 4D Flow velocity MAE by 1.2 percentage points and CFD velocity MAE by 0.69 percentage points, while maintaining competitive pointwise TDC error. Notably, PIC-Former outperforms LOWESS and Savitzky–Golay by 6.7 and 7.3 percentage points in velocity consistency, highlighting that curve-fitting accuracy alone does not guarantee hemodynamic validity. PIC-Former generates full-field parametric maps in 12.45 s, a 21.5× speedup over Gamma-variate fitting (268.27 s; 4.47 min), while improving accuracy.

We additionally performed a missing-frame stress test (Drop-20%) by randomly removing 20% of frames at inference time. PIC-Former degrades modestly (4D Flow velocity MAE 3.1%→3.4%) and remains superior to all competitors under the same setting, whereas Gamma-variate fitting deteriorates markedly (11.8%→14.5%).

Ablations confirm that both physics constraints and explicit Δt modeling are required for hemodynamic consistency: removing physics regularization de-

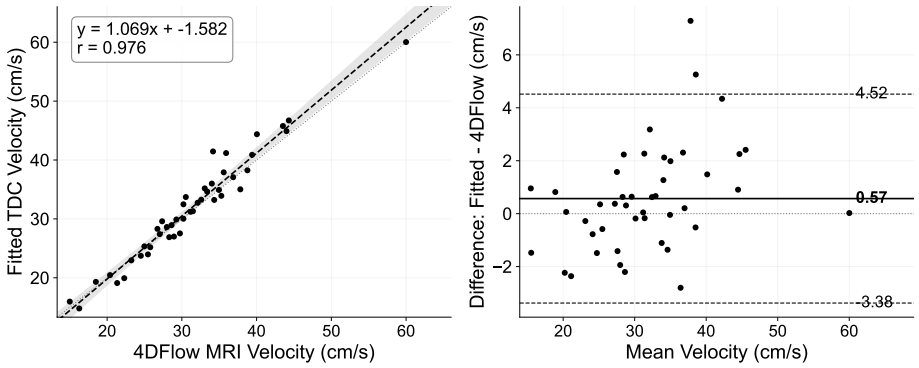

Fig. 2. Cross-modal validation of QDSA velocities derived from PIC-Former-reconstructed TDCs. Left: correlation with 4D Flow MRI reference velocities ($r = 0.976$). Right: Bland–Altman agreement plot (mean bias 0.57 cm/s; limits of agreement [-3.38, 4.52] cm/s).

grades velocity accuracy (+3.7%), while dropping Δt encoding speeds up inference (1.96 s) but worsens velocity consistency (+2.5%).

We further evaluated whether improved TDC reconstruction yields more reliable downstream transit time and velocity estimates. Fig. **??** shows strong agreement between 4D Flow MRI reference velocities and QDSA velocities derived from PIC-Former-reconstructed TDCs. The high correlation and near-zero mean bias indicate that the physics-inspired reconstruction preserves velocity ordering and magnitude across the physiological range. Because intra-arterial injection departs from native flow, SLS estimates a vessel-level transport speed; the 4D Flow agreement is thus read with the independent CFD reference, which is less affected by 4D Flow noise and large-vessel bias.

3.4 Qualitative and Mechanistic Assessment of Hemodynamic Parameters

As illustrated in Fig. **??**(a), the hemorrhagic case exhibits a marked intra-operative MTT increase within the aneurysm sac, whereas downstream territories show reduced or largely unchanged MTT, indicating a redistribution of transit time after intervention. We further evaluated mechanistic consistency with patient-specific CFD in Fig. **??**(b–c). The streamline patterns over the parent artery (PA), downstream branches, and aneurysm sac are qualitatively concordant in Fig. **??**(b), indicating that API captures the dominant flow organization resolved by CFD. At the PA location in Fig. **??**(c), the API-derived curve follows a smooth pulsatile trajectory and reproduces the overall CFD profile, while CFD resolves additional higher-frequency components due to its higher spatiotemporal fidelity. Together, these comparisons support the conclusion that physics-inspired TDC reconstruction yields clinically interpretable API maps and preserves bulk-flow behavior around the aneurysm inflow region.

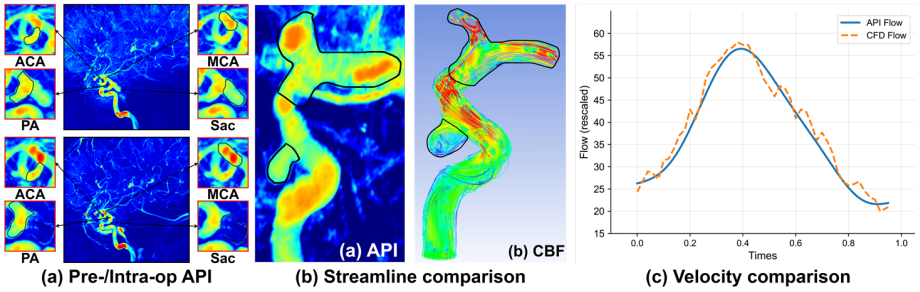

Fig. 3. Qualitative and CFD-based assessment of PIC-Former-derived hemodynamics in intracranial aneurysm interventions. (a) Pre- and intra-operative API MTT maps for a representative hemorrhagic outcome within clinically relevant ROIs (aneurysm sac, parent artery (PA), middle cerebral artery (MCA), and anterior cerebral artery (ACA)). (b) Velocity streamlines in the PA, downstream branches, and aneurysm sac estimated from API and patient-specific CFD. (c) Temporal flow profiles at the PA estimated from API and CFD.

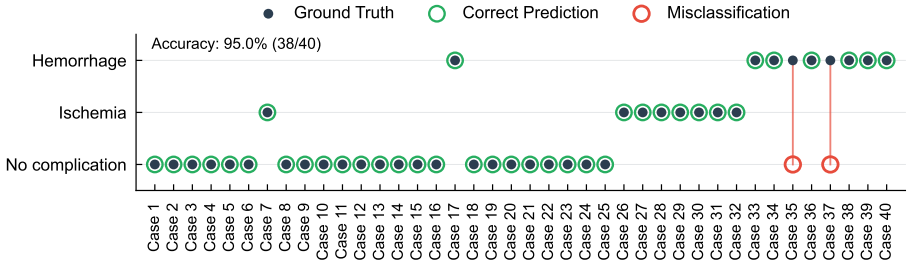

Fig. 4. Outcome prediction on the 40-case retrospective cohort using API-derived change features.

3.5 Clinical Utility and Intra-operative Risk Stratification

To evaluate the clinical relevance of PIC-Former, we conducted a retrospective risk stratification study on 40 cases following the protocol of [**?**] (25 complication-free, 7 ischemic events with diffusion-weighted imaging confirmation within 72 h, and 8 CT-confirmed hemorrhagic events). As shown in Fig. **??**, PIC-Former achieves 95.0% stratification accuracy (38/40), improving upon Gamma-variate-based reconstruction (87.5%, 35/40) under identical features and classifier settings. The physics-inspired reconstruction suppresses non-physiological oscillations that arise when fitting sparse irregular samples, rendering derived perfusion parameters less susceptible to fitting artifacts. This stability is clinically relevant because small perturbations in timing-sensitive indices can affect tissue-outcome prediction [**?**]. Consequently, mean transit time (MTT) and time-to-peak (TTP) extracted from PIC-Former reconstructions provide more reliable indicators for intra-operative risk stratification. Both misclassifications (Cases 35 and 37) were

complication-free studies assigned to a higher-risk category, reflecting a specificity limitation attributable to delayed post-interventional vessel-wall injury.

4 Conclusion

We present PIC-Former, a timestamp-conditioned continuous transformer for fast and sampling-robust hemodynamic reconstruction from irregularly sampled DSA in intracranial aneurysm interventions. By combining Δt-aware causal attention with physics-inspired regularization, PIC-Former reconstructs physiologically plausible TDCs that support stable API mapping and accurate QDSA velocity estimation under frame-rate variability and frame-drop perturbations. We validated hemodynamic consistency through cross-modal evaluation on paired DSA–4D Flow MRI data and independent patient-specific CFD, and further demonstrated improved intra-operative risk stratification using API-derived hemodynamic features. These results suggest that PIC-Former can serve as a practical building block toward real-time intra-operative hemodynamic assessment from routine DSA without additional acquisition or patient transfer; future work will focus on multi-center validation, broader cerebrovascular applications, and prospective deployment.

Acknowledgments. This work was supported in part by the National Natural Science Foundation of China (No. 62372441), the Guangdong Basic and Applied Basic Research Foundation (No. 2026B1515020093), the Shenzhen Science and Technology Program (Grant No. RCYX20231211090127030), and the Research Program of the Department of Education of Guangdong Province (Grant No. 2025ZDZX3027).

Disclosure of Interests. The authors declare no competing interests.

References

1. Chen, R.T., Rubanova, Y., Bettencourt, J., Duvenaud, D.K.: Neural ordinary differential equations. Advances in neural information processing systems **31** (2018)
2. Gaidzik, F., Korte, J., Saalfeld, S., Janiga, G., Berg, P.: Image-based hemodynamic simulations for intracranial aneurysms: the impact of complex vasculature. International Journal of Computer Assisted Radiology and Surgery **19**(4), 687–697 (2024)
3. Gong, Y., Cao, C., Guo, Y., Chang, B., Sheng, Z., Shen, W., Zou, Y., Lu, X., Xing, J., Xia, S.: Quantification of intracranial arterial stenotic degree evaluated by high-resolution vessel wall imaging and time-of-flight mr angiography: reproducibility, and diagnostic agreement with dsa. European Radiology **31**(8), 5479–5489 (2021)
4. Haouchine, N., Juvekar, P., Xiong, X., Luo, J., Kapur, T., Du, R., Golby, A.J., Frisken, S.F.: Estimation of high framerate digital subtraction angiography sequences at low radiation dose. In: Medical Image Computing and Computer Assisted Intervention – MICCAI 2021. Lecture Notes in Computer Science, vol. 12906, pp. 171–180. Springer (2021)
5. Hasani, R., Lechner, M., Amini, A., Liebenwein, L., Ray, A., Tschaikowski, M., Teschl, G., Rus, D.: Closed-form continuous-time neural networks. Nature Machine Intelligence **4**(11), 992–1003 (2022)

6. Kidger, P., Morrill, J., Foster, J., Lyons, T.: Neural controlled differential equations for irregular time series. Advances in neural information processing systems **33**, 6696–6707 (2020)
7. Korkmazer, B., Karaman, A.K., Ustundag, A., Arslan, S., Kızılkılıç, O., Koçer, N., Islak, C.: Magnetic resonance perfusion imaging findings following flow diversion in patients with complex middle cerebral artery bifurcation aneurysms: a single-center analysis regarding the jailed cortical branches. Journal of NeuroInterventional Surgery **16**(1), 8–14 (2024)
8. Lindner, T., Bolar, D.S., Achten, E., Barkhof, F., Bastos-Leite, A.J., Detre, J.A., Golay, X., Günther, M., Wang, D.J., Haller, S., et al.: Current state and guidance on arterial spin labeling perfusion mri in clinical neuroimaging. Magnetic resonance in medicine **89**(5), 2024–2047 (2023)
9. Liu, Z., Zhang, M., Gao, Y., Lv, J., Lu, F., Si, W.: Fast intra-operative angiographic parametric imaging for surgical outcome prediction of interventional cerebral aneurysms treatment. In: 2025 IEEE International Conference on Bioinformatics and Biomedicine (BIBM). pp. 2560–2567. IEEE (2025)
10. Liu, Z., Zhang, M., Wang, C., Wang, Z., Liao, X., Ou, C., Si, W.: Flow diverters treatment planning of small-and medium-sized intracranial saccular aneurysms on the internal carotid artery via constraint-based virtual deployment. International Journal of Computer Assisted Radiology and Surgery **19**(6), 1175–1183 (2024)
11. Ou, C., Li, C., Qian, Y., Duan, C.Z., Si, W., Zhang, X., Li, X., Morgan, M., Dou, Q., Heng, P.A.: Morphology-aware multi-source fusion–based intracranial aneurysms rupture prediction. European Radiology **32**(8), 5633–5641 (2022)
12. Ou, C., Qian, Y., Chong, W., Hou, X., Zhang, M., Zhang, X., Si, W., Duan, C.Z.: A deep learning–based automatic system for intracranial aneurysms diagnosis on three-dimensional digital subtraction angiographic images. Medical physics **49**(11), 7038–7053 (2022)
13. Rizk, J.: 4d flow mri applications in congenital heart disease. European radiology **31**(2), 1160–1174 (2021)
14. Scalzo, F., Liebeskind, D.S.: Perfusion angiography in acute ischemic stroke. Computational and Mathematical Methods in Medicine **2016**, 1–14 (2016)
15. Sel, K., Mohammadi, A., Pettigrew, R.I., Jafari, R.: Physics-informed neural networks for modeling physiological time series for cuffless blood pressure estimation. npj Digital Medicine **6**(1), 110 (2023)
16. Su, R., van der Sluijs, P.M., Marc, F.G., te Nijenhuis, F., Cornelissen, S.A.P., Roozenbeek, B., van Zwam, W.H., van der Lugt, A., Ruijters, D., Pluim, J., van Walsum, T.: perfdsa: Automatic perfusion imaging in cerebral digital subtraction angiography. International Journal of Computer Assisted Radiology and Surgery **20**(6), 1195–1203 (2025)
17. Uryga, A., Kasprowicz, M., Budohoski, K., Nasr, N., Czosnyka, M.: Predictive value of cerebrovascular time constant for delayed cerebral ischemia after aneurysmal subarachnoid hemorrhage. Journal of Cerebral Blood Flow & Metabolism **44**(7), 1208–1217 (2024)
18. Whitehead, J.F., Hoffman, C.A., Wagner, M.G., Periyasamy, S., Meram, E., Keller, M.E., Speidel, M.A., Laeseke, P.F.: Quantitative digital subtraction angiography measurement of arterial velocity at low radiation dose rates. CardioVascular and Interventional Radiology **47**(8), 1119–1126 (2024)
19. Wu, C., Davey, C., Sharma, G., Ng, F.: Resolving the overlap of macrovascular and microvascular flow components in digital subtraction angiography for cerebral reperfusion assessment. In: International Conference on Medical Image Computing and Computer-Assisted Intervention. pp. 528–537. Springer (2025)

20. Wu, Y., Shaughnessy, G., Hoffman, C.A., Oberstar, E.L., Schafer, S., Schubert, T., Ruedinger, K.L., Davis, B.J., Mistretta, C.A., Strother, C.M., et al.: Quantification of blood velocity with 4d digital subtraction angiography using the shifted least-squares method. American Journal of Neuroradiology **39**(10), 1871–1877 (2018)
21. Xu, Z., Zhao, H., Cui, Z., Liu, W., Zheng, C., Wang, X.: Most-dsa: Modeling motion and structural interactions for direct multi-frame interpolation in dsa images. In: ECAI 2024. Frontiers in Artificial Intelligence and Applications, vol. 392, pp. 537–544. IOS Press (2024)
22. Zhu, H., Zhang, Y., Li, C., Ma, C., Liang, F., Liang, S., Jiang, P., Jiang, C.: Quantitative evaluation of the hemodynamic differences between ruptured and unruptured cerebral arteriovenous malformations using angiographic parametric imaging–derived radiomics features. Neuroradiology **65**(1), 185–194 (2023). https://doi.org/10.1007/s00234-022-03030-8, https://doi.org/10.1007/s00234-022-03030-8